



Cite this: DOI: 10.1039/d2cp02059a

Electric field and strain engineering tuning Rashba spin splitting in quasi-one-dimensional organic–inorganic hybrid perovskites (MV)Al₃Cl₂ (MV = methylviologen, A = Bi, Sb)†

 Chao Wang,^a Shouyu Wang,^{*b} Zhifeng Xiao,^b Winnie Wong-Ng,^c Wei Zhou ^a and Weifang Liu ^{*a}

We systematically study the Rashba spin texture of lead-free quasi-one-dimensional organic–inorganic hybrid perovskites (OIHP), (MV)Al₃Cl₂ (MV = methylviologen, A = Bi, Sb) with first-principles calculations. The k_x – k_y plane Rashba spin splitting was found to depend on the composition of Bi (Sb) and I atoms at band edges. Importantly, increasing ferroelectric polarization and the stretch along the z-direction can effectively enhance the amplitude of the Rashba spin splitting. This work provides an avenue for electric field and strain-controlled spin splitting and highlights the potential of quasi-one-dimensional OIHP for further applications in spin field effect transistors and photovoltaic cells.

 Received 6th May 2022,
Accepted 1st July 2022

DOI: 10.1039/d2cp02059a

rsc.li/pccp

1 Introduction

The organic–inorganic hybrid perovskites (OIHP) belong to one of the most versatile family of materials in the fields of energy and information technology due to their attractive photovoltaic and magneto-optical properties.^{1,2} Recent investigation of OIHP CH₃NH₃PbI₃ illustrated a spin relaxation lifetime of about 7 ps due to the presence of the Rashba effect.³ The Rashba effect is the spin splitting of the energy band due to the asymmetry of the structural space reversal and the spin–orbit coupling (SOC).⁴ Materials can possess a high optical absorption coefficient under the Rashba effect.^{5,6} In addition, a photogenerated electron under the Rashba effect can flip its spin into the opposite spin band structure, as a result of spin forbidden recombination, so as to prolong spin relaxation lifetime. The Rashba spin texture can be easily controlled by an electric field, holding promise for the development of spin field-effect-transistors (FETs).^{7,8} Recently, numerous papers have reported the Rashba effect in various ferroelectric OIHP, including (4AMP)PbI₄⁹ and (PEA)₂PbI₄.¹⁰ However, recent research on the Rashba effect in perovskites has been mainly

based on the toxic heavy metal Pb, which causes environmental problems and hinders large-scale industrialization of materials.^{10,11} Thus, research of lead-free alternatives is critical to the development of perovskite based photovoltaic cells and spin FETs.

The Bi- and Sb-based OIHP have been research hotspots in the field of optoelectronics to replace Pb OIHP.¹² Importantly, the Bi-based OIHP is more stable than that of Pb-based OIHP under an atmosphere.^{13,14} As adjacent cations in the periodic table, Bi³⁺ and Pb²⁺ have very similar ionic radius and the same electronic configuration 6s²6p⁰. Low-dimensional ferroelectric materials including heavy Bi and Pb atoms possess similar Rashba constants, for example, BiTeBr (1.28 eV Å)¹⁵ and bilayer PbTe (1.05 eV Å).¹⁶ Recently, quasi-one-dimensional ferroelectric OIHP (MV)Al₃Cl₂ (MV = methylviologen (C₁₂H₁₄Cl₂N₂), A = Bi, Sb) have shown their potential applications in photovoltaic and high-density ferroelectric memory areas due to their high electron transport, low coercive field and strong optical absorption properties.^{17–19} More importantly, large-scale (MV)Al₃Cl₂ was synthesized using the hydrothermal method and the Curie temperature (T_c) of the ferroelectric phase was above room temperature.^{20,21} These two advantages are conducive to the operation of devices at room temperature. Since SOC plays an important role for heavy metals Bi, Sb and I, the Rashba effect is expected to be realized for ferroelectric OIHP (MV)Al₃Cl₂.

Here, we systematically investigated the Rashba effect on lead-free quasi-one-dimensional ferroelectric OIHP (MV)Al₃Cl₂ with density functional theory (DFT). As a result of the SOC effect, polar (MV)Al₃Cl₂ exhibits intrinsic Rashba spin splitting

^a Tianjin Key Laboratory of Low Dimensional Materials Physics and Preparing Technology, School of Science, Tianjin University, Tianjin 300072, China. E-mail: wfliu@tju.edu.cn; Tel: +86-22-27406852

^b College of Physics and Material Science, Tianjin Normal University, Tianjin 300074, China. E-mail: shouyu.wang@yahoo.com

^c Materials Measurement Science Division, National Institute of Standards and Technology, Gaithersburg, Maryland 20899, USA

† Electronic supplementary information (ESI) available. See DOI: <https://doi.org/10.1039/d2cp02059a>

at the Γ points and larger Rashba constants (180 meV Å for (MV)Bi₃Cl₂ and 123 meV Å for (MV)Sb₃Cl₂) compared with experimentally measured data for GaSb/InAs/GaSb (81 meV Å)²² and GaSb/InAs (90 meV Å).^{23,24} The Rashba spin textures are located on the conduction band minimum (CBM) of (MV)Bi₃Cl₂. However, the CBM and valence band maximum (VBM) of (MV)Sb₃Cl₂ both possess Rashba-type spin texture. The Rashba constants can be adjusted by ferroelectric polarization. The applied stress along the z -direction modulates the contribution of atomic orbitals to both the CBM and VBM. This strategy provides a new route for the design of the next generation spin devices.

2 Calculation details and Rashba module

All calculations were performed based on density functional theory (DFT) with the Vienna *ab initio* Simulation Package (VASP).^{25–27} The structural and electronic properties were adopted with the projector-augmented-wave (PAW) method and the generalized gradient approximation parameterized with Perdew–Burke–Ernzerhof (GGA-PBE).²⁸ The cutoff energy of the electronic plane wave is 500 eV and the convergence of total energy calculations was set at $<10^{-6}$ eV per atom. The Brillouin zone was sampled with $3 \times 3 \times 3$ and $4 \times 4 \times 4$ Monkhorst–Pack k -points grids for geometry optimization and self-consistent calculations, respectively. All atomic coordinates and lattice constants were optimized until all residual forces were <0.01 eV Å⁻¹. The Heyd–Scuseria–Ernzerhof (HSE06) hybrid functional was also crosschecked to calculate the electronic band structures.^{29,30} The spin–orbit coupling (SOC) effect was considered to investigate Rashba constants. The Rashba constants with both PBE and HSE06 methods are similar, as shown in Fig. S1 of the ESI,[†] indicating the HSE06 functional does not affect the amplitude of the Rashba spin splitting.^{31,32} Then, the Rashba constants for all subsequent calculations were adopted by using the PBE + SOC method. The ferroelectric polarization was calculated with the Berry phase method.³³

Referring to the Kramers degeneracy theorem, the electronic states with spin-up and -down are degenerate in a system with high space reversal and time reversal symmetry (Fig. 1(a)).³⁴ In the presence of an asymmetric spatial structure and SOC, the spin degeneracy can be relieved to form the Rashba effect, as shown in Fig. 1(b) and (c). When the spatial inversion is asymmetric along the z -direction, the k_x – k_y plane spin will split under the SOC effect, as shown in Fig. 1(d) and (e). The Hamiltonian can be defined as the following:³⁵

$$H = \frac{p^2}{2m^*} + \alpha_R(\sigma \times k)\hat{z} \quad (1)$$

where m^* , α_R , σ , k and \hat{z} represent the electron effective mass, the Rashba constant, the Pauli matrix, the electron wave vector, and the surface normal, respectively. The eigenvalues for the

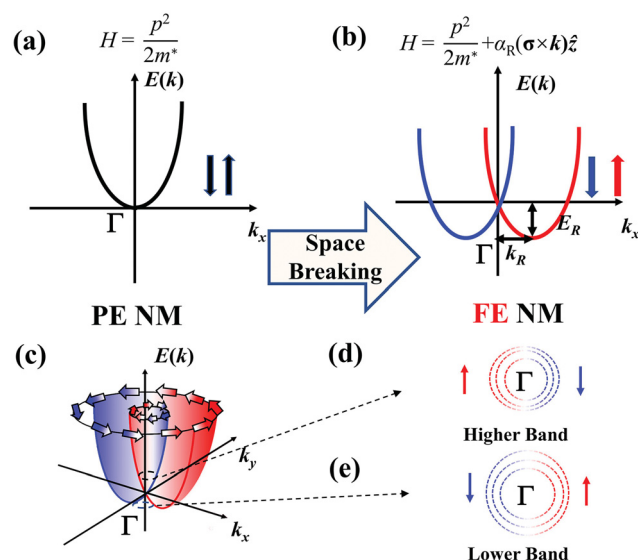


Fig. 1 The schematic structure of the spin splitting band for systems (a) paraelectric and non-magnetic, and (b) ferroelectric and non-magnetic. (c) 3D Schematic illustrations of the Rashba effect. The characteristic spin texture of the (d) higher and (e) lower conduction band minimum at the Γ point. The red and blue colors show spin-up and -down states, respectively.

Rashba effect are:³⁶

$$E_{\pm}(k) = \frac{\hbar^2 k^2}{2m^*} \pm \alpha_R k = \frac{\hbar^2}{2m^*}(k^2 + k_R)^2 - E_R \quad (2)$$

where $k = k(\cos \theta, \sin \theta, 0)$ stands for a vector at the k_x – k_y plane. The + and – represent the higher and lower conduction band minimum at the Γ point, respectively. The Rashba energy (E_R) and the Rashba momentum (k_R) were directly estimated in the band structure. Then, we use the Rashba constant (α_R) as the following equation:

$$\alpha_R = \frac{2E_R}{k_R} \quad (3)$$

3 Results and discussion

3.1 Crystal and electronic structure

The quasi-one-dimensional ferroelectric OIHP (MV)Al₃Cl₂ are polar tetragonal structures with space group $P4nc$ (No. 104), where large organic molecules MV separate inorganic octahedrons Al₃Cl₂, as shown in Fig. 2(a). Additionally, the crystal structure along the x - and y -direction is symmetrical. However, the crystal structure along the z -direction is asymmetric, as shown in Fig. 2(b), suggesting the polar axis is the z -direction. Obviously, the off-center A atoms of the two inorganic octahedrons Al₃ and AlCl₂ play a significant role in the space inversion asymmetry of the Al₃Cl₂ octahedrons, resulting in misalignment of the positive and negative charge centers. The optimized structural parameters ($a = b = 12.34$ Å, $c = 12.89$ Å for (MV)Bi₃Cl₂; $a = b = 12.29$ Å, $c = 12.85$ Å for (MV)Sb₃Cl₂) are in good agreement with the experimental data.^{20,21} The symmetrical

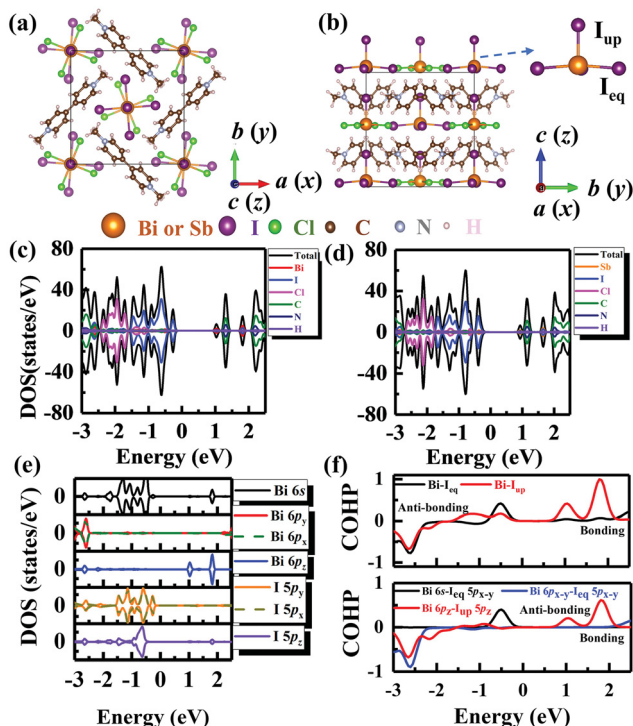


Fig. 2 (a) The top and (b) side views of organic–inorganic hybrid perovskites $(MV)Al_3Cl_2$ ($A = Bi, Sb$) structures. The total and projected density of states (DOS) of (c) $(MV)BiI_3Cl_2$ and (d) $(MV)SbI_3Cl_2$, respectively. (e) The projected DOS of Bi and I atoms. (f) The Crystal Orbital Hamilton Population (COHP) of Bi and its neighboring I atoms.

spins up and down density of states (DOS) of $(MV)Al_3Cl_2$ exhibit non-magnetic characteristics, which means that the time reversal is symmetrical, as shown in Fig. 2(c) and (d). Thus, OIHP $(MV)Al_3Cl_2$ are polar non-magnetic semiconductors.

The valence band maximum (VBM) and conduction band minimum (CBM) of $(MV)Al_3Cl_2$ mainly originate from the orbital hybridization between A and I atoms in the polar inorganic octahedrons. Within the polar octahedrons, there are two types of I anions surrounding the A^{3+} cation which are marked as upper (I_{up}) and equator (I_{eq}) with reference to the center A^{3+} cation (Fig. 2(b)). In order to investigate the atomic orbital and bonding states between A and I atoms, the projected DOS and Crystal Orbital Hamilton Population (COHP) were calculated as shown in Fig. 2(e), (f) and Fig. S2 of the ESI.† Since the two outer atomic orbitals of Bi atoms are 6s and 6p, orbital hybridization between Bi^{3+} cations and I^- anions at the band structure edge are mainly Bi 6s–I 5p and Bi 6p–I 5p. The DOS of Bi-6s and I-5p are mainly located at the valence band from -1.9 eV to 0 eV. Combining with the results of COHP (Fig. 2(f)), the VBM is mainly contributed by the anti-bonding states between Bi-6s and I_{eq} -5p $_{x-y}$ near the Fermi-level. On the other hand, Bi-6p $_z$ and I-5p $_z$ were located in the conduction band at about 1.0 eV and 1.7 eV of the DOS. As shown in Fig. 2(f), the anti-bonding states between Bi-6p $_z$ and I_{up} -5p $_z$ have main peaks around 1.0 eV and 1.7 eV, respectively. Thus, the CBM above the Fermi-level is mainly contributed by the anti-bonding states between Bi-6p $_z$ and I_{up} -5p $_z$. In summary, the VBM is controlled by the orbital

hybridization between Bi-6s and I_{eq} -5p $_{x-y}$, while the CBM is contributed by the orbital hybridization between Bi-6p $_z$ and I_{up} -5p $_z$. Similarly, for $(MV)SbI_3Cl_2$, the VBM is contributed by the orbital hybridization between Sb-5s and I_{eq} -5p $_{x-y}$, however, the CBM is contributed by Sb-5p $_z$ and I_{up} -5p $_z$ (Fig. S2, ESI†).

3.2 Rashba effect and splitting

The band structures of $(MV)BiI_3Cl_2$ with and without the SOC effect were calculated in Fig. 3(a). In the band structure without the SOC effect, both VBM and CBM located at the Γ -point indicates a direct band gap. Due to the SOC effect on the heavy Bi and I atoms for $(MV)BiI_3Cl_2$, the band gap reduces and the spin degeneracy states at the CBM are removed. This indicates that the SOC effect cannot be ignored. Without the SOC effect, the Rashba band splitting of the CBM is from the Γ point to the X point and from the Γ point to the M point, as shown in Fig. 3(b). To understand the role of electrons in band splitting, the electron density of states on the CBM at the Γ point was calculated as shown in Fig. 3(c). The electron density of the CBM at the Γ point was mainly concentrated on the Bi and I atoms of BiI_3Cl_2 chains. On the basis of the aforementioned analysis for the CBM and VBM, the schematic diagram of atomic orbital bonding was plotted in Fig. 3(d). The CBM was composed by anti-bonding states between Bi-6p $_z$ and I_{up} -5p $_z$ orbitals. Therefore, such Rashba band splitting can be contributed to by the Bi-6p $_z$ and I_{up} -5p $_z$ orbitals of the CBM.

On the basis of the calculated Rashba energy ($E_{\Gamma-X} = 2.50$ meV; $E_{\Gamma-M} = 3.52$ meV) and Rashba momentum ($k_{\Gamma-X} = 27.78$ m \AA^{-1} ; $k_{\Gamma-M} = 48.22$ m \AA^{-1}) for $(MV)BiI_3Cl_2$, according to eqn (3), the Rashba constants $\alpha_{\Gamma-X}$ and $\alpha_{\Gamma-M}$ were calculated to be 180 meV \AA and 146 meV \AA , respectively, which are larger than the experimental measured 20 meV \AA for $LaAlO_3/SrTiO_3$ interface and 70 meV \AA for InGaAs/InAlAs heterostructure.^{37,38} The anisotropy of Rashba originates from the spatial symmetry of $(MV)Al_3Cl_2$ (tetragonal system). The same phenomenon is also observed in two-dimensional materials with out-of-plane polarization, layered heterostructures, or interfaces.^{39–41}

To observe the characteristics of Rashba spin splitting in $(MV)BiI_3Cl_2$, the 2D spin textures of the lower and upper CBM bands on the Γ point centered in the k_x – k_y plane are plotted, as shown in Fig. 3(e) and (f). The black arrows represent the k_x – k_y plane vector components of the spin texture, and the blue and red gradients represent k_z vector components of the spin texture. It can be clearly seen that the spin arrow in the lower CBM band rotates clockwise, while the spin arrow in the higher CBM band rotates counterclockwise, which visually confirms the characteristics of Rashba splitting.⁴² In addition, the squares branched inside and outside the split zone also highlight the splitting of the anisotropic zone of the orthorhombic system. For visual representation, the 3D band structures of the lower and higher CBM bands at the Γ -point are shown in Fig. 3(g).

The band structures of $(MV)SbI_3Cl_2$ without and with the SOC effect were calculated in Fig. 4(a). In the band structure with the SOC effect, the VBM and CBM are located at the Γ point and M point, respectively, indicating an indirect band gap.

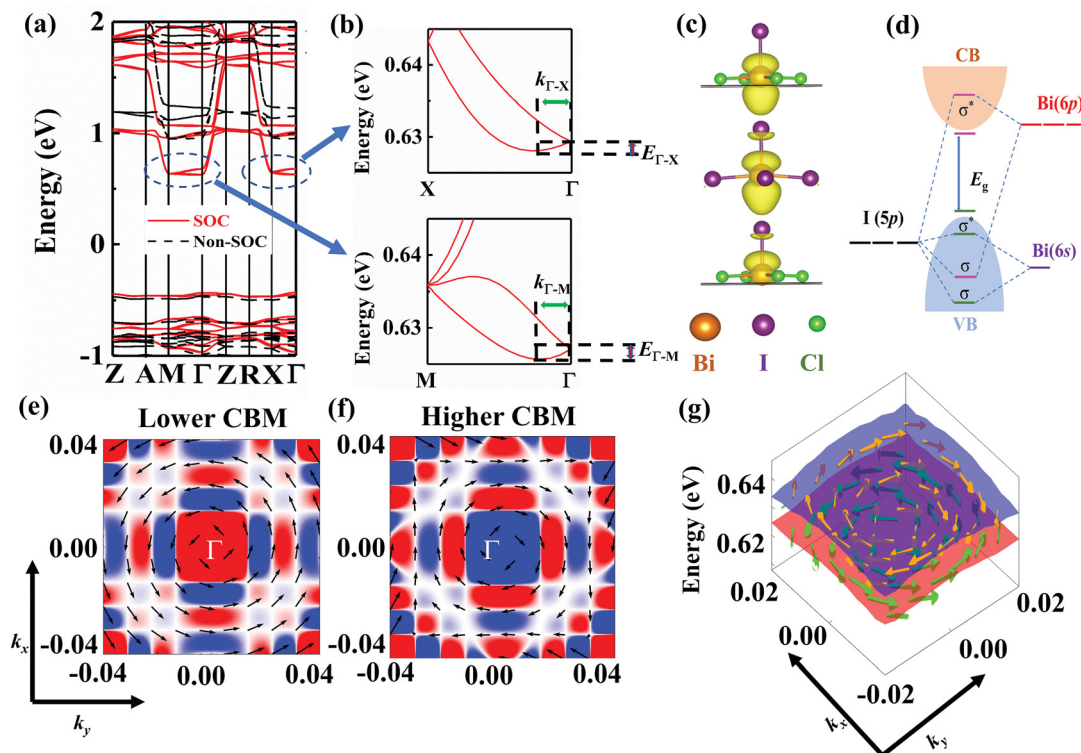


Fig. 3 (a) The band structure of (MV)Bi₃Cl₂ with and without the SOC effect. (b) The spin splitting energy of the CBM along the Γ to X point and the Γ to M point. (c) The charge density of the conduction band minimum (CBM) at the Γ -point. (d) Schematic diagram of the bonding states of Bi and I atomic orbitals. Spin texture of the (e) lower and (f) higher CBM bands at the Γ -point, where the black arrows represent the k_x - k_y vector components, and the blue and red gradients represent the k_z vector components. (g) 3D spin texture of the lower and higher CBM bands at the Γ -point.

Within the ferroelectric structure and SOC effect of Sb and I atoms, different from the Bi system, it was observed for the Sb system that the Rashba-type spin-splitting effect of the k_x - k_y plane is located at the VBM and CBM, as shown in Fig. 4(b) and (c). The Rashba constants of VBM (α_V) and CBM (α_C) are 121 meV Å and 123 meV Å, respectively. The spin textures of the VBM and CBM are plotted at the Γ point and M point, respectively, as shown in Fig. 4(d) and (e). According to calculated results of hybridization between Sb and I atoms in Fig. S2 of the ESI,[†] and based on the similar analysis of the Bi system mentioned above, the VBM is mainly composed of the anti-bonding states between Sb-5s and I_{eq}-5p_{x-y} orbitals, while the CBM is composed of the anti-bonding states between Sb-5p_z and I_{up}-5p_z orbitals. Importantly, the small electron density of the VBM at the Γ point is along the z direction, as shown in Fig. S3 of the ESI,[†] forming Rashba spin splitting of the VBM at the Γ point.

3.3 Rashba effect with polarization

In addition to the SOC effect of heavy metals, we further investigated the role of ferroelectric polarization on the Rashba effect. Corresponding with the ferroelectric phase (*P4nc*), the paraelectric (PE) phase of (MV)Al₃Cl₂ possesses the space group *P4/mnc* (No. 128),¹⁹ where the A atom is located in the center of the two octahedrons Al₃ and AlCl₂, as shown in Fig. 5(a). Inorganic octahedrons play a key role in the regulation of

band edges. During phase transition, the octahedral distortion originates from the decentering of the central A atom along the z-axis direction, marked as the bond angle (θ) between the I and A atoms in the plane, as shown in Fig. 5(b). The bond angle of the Bi (Sb) system decreases from 180° for the paraelectric phase (θ_{PE}) to 170° (175°) for the ferroelectric phase (θ_{FE}). The Rashba constant gradually increases with the ferroelectric polarization until it reaches the maximum value,⁴³ as shown in Fig. 5(c) and Fig. S4 of the ESI,[†] suggesting that the extra electric field can tune the Rashba-type spin splitting of (MV)Al₃Cl₂. It was reported that (MV)Bi₃Cl₂ has a small coercive field ($E_c \approx 0.1$ – 0.2 kV cm⁻¹),²¹ so the Rashba effect should be easily manipulated by an external electric field, with potential for applications in spin field effect transistors.

In order to further understand the mechanism of ferroelectric polarization dependent on the Rashba effect, we calculated the contribution of I-5p_z and Bi-6p_z orbitals for the CBM with phase transition for that CBM mainly originating from antibonding states of the I-5p_z and Bi-6p_z orbitals, as shown in Fig. 5(d). In the paraelectric phase, the Bi-6p_z dominates the CBM. A small part of the CBM is composed of I-5p_z. As the ferroelectric polarization increases, the contribution of Bi-6p_z to the CBM gradually decreases, while the contribution of I-5p_z to the CBM gradually increases, indicating that the electrons on Bi-6p_z are transferred to the I-5p_z atom, leading to the coupling

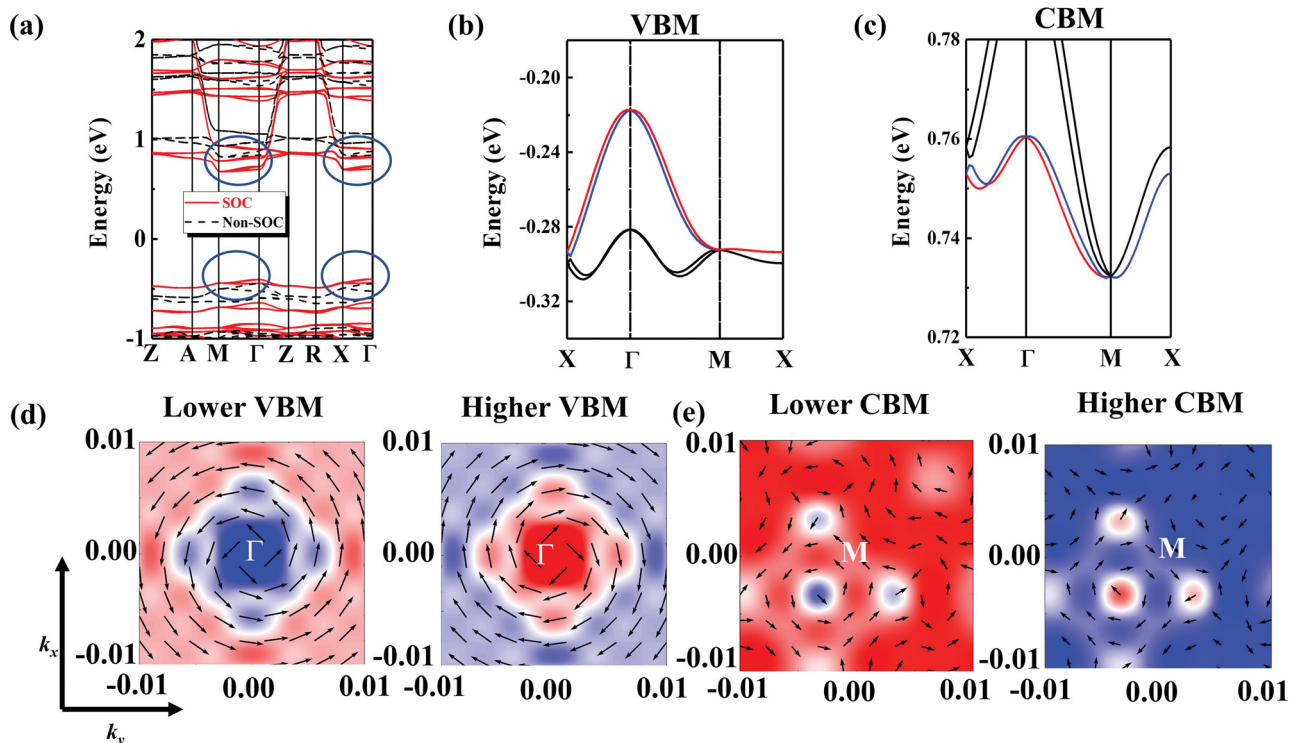


Fig. 4 (a) The band structure of (MV)SbI₃Cl₂ without and with the SOC effect. (b) The band structure of the k_x - k_y plane valence band maximum (VBM). (c) The band structure of the k_x - k_y plane conduction band minimum (CBM). (d) The spin textures of the lower and higher VBM bands at the Γ -point. (e) The spin textures of the lower and higher CBM bands at the M -point. The red and blue gradients represent the k_z vector components.

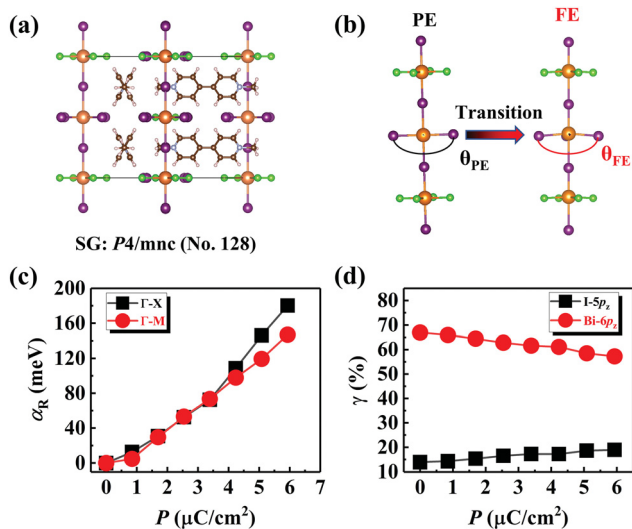


Fig. 5 (a) The paraelectric phases of (MV)Al₃Cl₂ with space group $P4/mnc$ (No. 128). (b) The angles of the I-A-I bonds with the paraelectric (θ_{PE}) to ferroelectric phase (θ_{FE}) transition. (c) The Rashba constant (α_R) and (d) atomic orbital contribution (γ) of (MV)BiI₃Cl₂ with transition from the paraelectric phase to ferroelectric phase.

strengthening between the Bi and I atoms along the z -direction, which causes the SOC to strengthen. The polarization along the z -direction enhances the interaction between the atoms along the z direction, thereby increasing the Rashba constant.

3.4 Rashba effect with strain engineering

A ferroelectric material is a type of piezoelectric material that produces an electric field between two ends when subjected to pressure. Strain engineering is an effective method to tune the Rashba-type spin splitting. The Rashba constants of (MV)Al₃Cl₂ strain engineering ($\varepsilon = (c - c_0)/c$) from -3% to 3% along the z direction were calculated, as shown in Fig. 6(a) and (b). Considering the orbital contribution of the CBM, Bi-6 p_z is gradually increasing, while I-5 p_z is gradually decreasing, as shown in Fig. 6(c) and (d). This appearance indicates that the I-5 p_z orbital plays an important role for the Rashba effect, which is similar to the d_{z^2} controlling Rashba coupling in the 1T-phase Janus WSSe monolayers.⁴⁴ However, in the VBM of (MV)SbI₃Cl₂, the Rashba constant and the z -direction strain are negatively correlated. The contributions of Sb-5 p_z and I-5 p_z to the VBM gradually decrease, leading to the reduction of p-p orbital coupling between Sb and I atoms in the z direction as shown in Fig. 6(d). Hence, the contribution of I-5 p_z to the VBM and CBM can regulate the spin-orbit coupling strength. In addition, we calculated the change rate (η) of the Rashba constant for (MV)Al₃Cl₂. η is defined as follows:

$$\eta = \Delta\alpha_R/\Delta\varepsilon \quad (4)$$

$$\Delta\alpha_R = \alpha_{R|\varepsilon=1\%} - \alpha_{R|\varepsilon=-1\%} \quad (5)$$

where ε represents the strain constant. The η of the CBM on (MV)BiI₃Cl₂ is 70 meV \AA , which is much larger than that of the

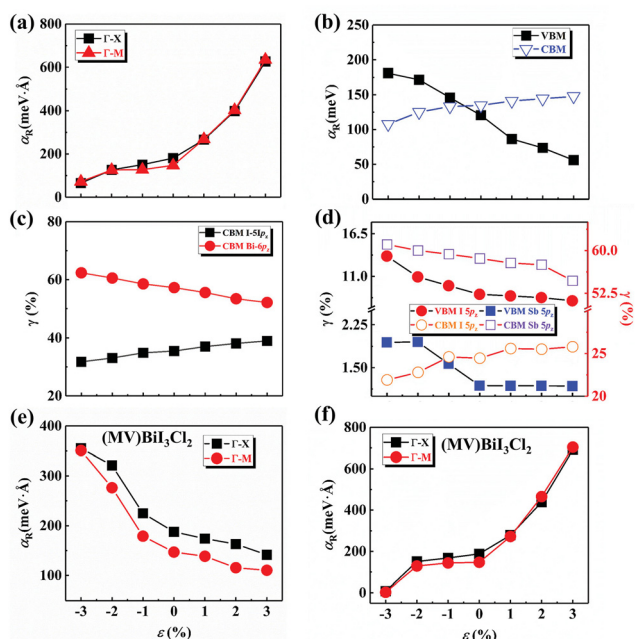


Fig. 6 The Rashba constants of (a) (MV)BiI₃Cl₂ and (b) (MV)SbI₃Cl₂ with strain engineering from -3% to 3% along the z direction. Total orbital contribution of individual atoms in (c) (MV)BiI₃Cl₂ and (d) (MV)SbI₃Cl₂ to the conduction band minimum (CBM) and valence band maximum (VBM) at the Γ -point under different magnitudes of z direction strain. (e) The Rashba effect of CBM on (MV)BiI₃Cl₂ with biaxial in-plane strain engineering from -3% to 3% . (f) The Rashba effect of CBM on (MV)BiI₃Cl₂ with bulk strain engineering from -3% to 3% .

CBM on (MV)SbI₃Cl₂ (4 meV \AA). However, the η of the VBM on (MV)SbI₃Cl₂ is 30 meV \AA . These results indicate that strain along the z direction is an effective way to modulate the large amplitude of Rashba constants by the contribution of I-5p_z orbitals.

For the z direction and the k_x - k_y plane in a competitive state, we found a positive correlation between the Rashba constant and the bulk strain, as shown in Fig. 6(e) and (f). The Rashba constant depends on the z -direction. In addition, the tension increases the lattice constant in real space, which in turn reduces the momentum offset (k_R) in the reciprocal momentum space. According to eqn (4), the smaller the momentum offset, the stronger the spin-orbit coupling. In the case of a 3% stretch, the Rashba constant of (MV)BiI₃Cl₂ (704 meV \AA) is more than 3 times that of the normal state. Therefore, stretching is an effective way to adjust the spin splitting of materials. The next generation of self-powered spintronic devices requires the channel semiconductor material to possess a high-voltage electrical coefficient and huge Rashba split, which can be effectively modulated by external disturbances such as strain engineering or electric fields. Taking all these aspects into consideration, it is found that non-lead organic-inorganic hybrid perovskite (MV)AlI₃Cl₂ is the most suitable candidate because it meets all these criteria and can be expected under strain engineering to produce (MV)AlI₃Cl₂-based spintronic devices.

4 Conclusions

Based on first principles calculation with DFT theory, we investigated the Rashba effect of lead-free OIHP (MV)AlI₃Cl₂. Under the effect of spin-orbit coupling, the Rashba-type spin textures are the CBM of (MV)BiI₃Cl₂ and the CBM and VBM of (MV)SbI₃Cl₂. Due to the symmetry of the tetragonal system, the Rashba constants of (MV)BiI₃Cl₂ and of (MV)SbI₃Cl₂ are anisotropic. In the ferroelectric phase transition, the magnitude of the Rashba constant increases with the increase in polarization. The strength of the Rashba spin-orbit coupling mainly originates from the I-5p_z orbital. Under the condition of z -axis stretching, the contribution of the I-5p_z orbital to (MV)AlI₃Cl₂ increases, resulting in the enhancing of the Rashba constant of the CBM. However, the stretching effect on the Rashba constants of the VBM is opposite to that of the CBM. Therefore, under stretched conditions, (MV)AlI₃Cl₂ can replace Pb-containing Rashba spintronic devices.

Author contributions

Chao Wang: data curation, investigation, writing – original draft, writing – review & editing. Shouyu Wang: writing – review & editing. Zhifeng Xiao: writing – review & editing. Winnie Wong-Ng: supervision, writing – review & editing. Wei Zhou: writing – review & editing. Weifang Liu: resources, supervision, writing – review & editing.

Conflicts of interest

There are no conflicts to declare.

Acknowledgements

This work was partially funded by the National Natural Science Foundation of China (51572193), and the Natural Science Foundation of Tianjin (20JCZDJC00210). Most calculations were performed at the National Supercomputer Center in Tianjin.

References

- 1 L. Mao, C. C. Stoumpos and M. G. Kanatzidis, *J. Am. Chem. Soc.*, 2019, **141**, 1171–1190.
- 2 J. Wang, C. Zhang, H. Liu, R. McLaughlin, Y. Zhai, S. R. Vardeny, X. Liu, S. McGill, D. Semenov and H. Guo, *et al.*, *Nat. Commun.*, 2019, **10**, 1–6.
- 3 D. Giovanni, H. Ma, J. Chua, M. Gratzel, R. Ramesh, S. Mhaisalkar, N. Mathews and T. C. Sum, *Nano Lett.*, 2015, **15**, 1553–1558.
- 4 E. I. Rashba, *Phys. Rev. B: Condens. Matter Mater. Phys.*, 2000, **62**, R16267.
- 5 H. L. Kagdada, S. K. Gupta, S. Sahoo and D. K. Singh, *J. Phys. Chem. Lett.*, 2020, **11**, 7679–7686.
- 6 L. Martiradonna, *Nat. Mater.*, 2018, **17**, 377.

- 7 M. Kepenekian and J. Even, *J. Phys. Chem. Lett.*, 2017, **8**, 3362–3370.
- 8 K. Leng, R. Li, S. P. Lau and K. P. Loh, *Trends Chem.*, 2021, **3**, 716–732.
- 9 J. Yin, R. Naphade, P. Maity, L. Gutiérrez-Arzaluz, D. Almalawi, I. S. Roqan, J. L. Brédas, O. M. Bakr and O. F. Mohammed, *Nat. Commun.*, 2021, **12**, 1–9.
- 10 I. H. Park, Q. Zhang, K. C. Kwon, Z. Zhu, W. Yu, K. Leng, D. Giovanni, H. S. Choi, I. Abdelwahab and Q. H. Xu, *et al.*, *J. Am. Chem. Soc.*, 2019, **141**, 15972–15976.
- 11 J. Yin, P. Maity, L. Xu, A. M. El Zohry, H. Li, O. M. Bakr, J.-L. Brédas and O. F. Mohammed, *Chem. Mater.*, 2018, **30**, 8538–8545.
- 12 Z. Shi, J. Guo, Y. Chen, Q. Li, Y. Pan, H. Zhang, Y. Xia and W. Huang, *Adv. Mater.*, 2017, **29**, 1605005.
- 13 K. Eckhardt, V. Bon, J. Getzschmann, J. Grothe, F. M. Wisser and S. Kaskel, *Chem. Commun.*, 2016, **52**, 3058–3060.
- 14 B.-W. Park, B. Philippe, X. Zhang, H. Rensmo, G. Boschloo and E. M. J. Johansson, *Adv. Mater.*, 2015, **27**, 6806–6813.
- 15 Y.-z. Jia, W.-x. Ji, C.-w. Zhang, S.-f. Zhang, P. Li and P.-j. Wang, *RSC Adv.*, 2017, **7**, 11636–11643.
- 16 C. Liu, H. Gao, Y. Li, K. Wang, L. A. Burton and W. Ren, *J. Mater. Chem. C*, 2020, **8**, 5143–5149.
- 17 C. Wang, Y. Lei, W. Wong-Ng, Q. Gu, X. Wu, W. Zhou, S. Wang and W. Liu, *Phys. Rev. B: Condens. Matter Mater. Phys.*, 2021, **104**, 075138.
- 18 Y. Lei, S. Wang, S. Ma, Y. Shi, D. Fu and W. Liu, *Appl. Phys. Lett.*, 2019, **114**, 182902.
- 19 Y. Lei, S. Wang, J. Xing, H. Xu, J. Han and W. Liu, *Inorg. Chem.*, 2020, **59**, 4349–4356.
- 20 N. Leblanc, N. Mercier, M. Allain, O. Toma, P. Auban-Senzier and C. Pasquier, *J. Solid State Chem.*, 2012, **195**, 140–148.
- 21 N. Leblanc, N. Mercier, L. Zorina, S. Simonov, P. Auban-Senzier and C. Pasquier, *J. Am. Chem. Soc.*, 2011, **133**, 14924–14927.
- 22 K. S. Cho, T.-Y. Huang, H.-S. Wang, M.-G. Lin, T.-M. Chen, C.-T. Liang, Y. F. Chen and I. Lo, *Appl. Phys. Lett.*, 2005, **86**, 222102.
- 23 J. Luo, H. Munekata, F. F. Fang and P. J. Stiles, *Phys. Rev. B: Condens. Matter Mater. Phys.*, 1990, **41**, 7685–7693.
- 24 J. Luo, H. Munekata, F. F. Fang and P. J. Stiles, *Phys. Rev. B: Condens. Matter Mater. Phys.*, 1988, **38**, 10142–10145.
- 25 G. Kresse and J. Furthmüller, *Phys. Rev. B: Condens. Matter Mater. Phys.*, 1996, **54**, 11169–11186.
- 26 G. Kresse and J. Furthmüller, *Comput. Mater. Sci.*, 1996, **6**, 15–50.
- 27 P. E. Blöchl, *Phys. Rev. B: Condens. Matter Mater. Phys.*, 1994, **50**, 17953–17979.
- 28 J. P. Perdew, K. Burke and M. Ernzerhof, *Phys. Rev. Lett.*, 1996, **77**, 3865–3868.
- 29 J. Heyd, G. E. Scuseria and M. Ernzerhof, *J. Chem. Phys.*, 2003, **118**, 8207–8215.
- 30 J. Heyd, G. E. Scuseria and M. Ernzerhof, *J. Chem. Phys.*, 2006, **124**, 219906.
- 31 P. A. L. Sino, L.-Y. Feng, R. A. B. Villaos, H. N. Cruzado, Z.-Q. Huang, C.-H. Hsu and F.-C. Chuang, *Nanoscale Adv.*, 2021, **3**, 6608–6616.
- 32 L. Leppert, S. E. Reyes-Lillo and J. B. Neaton, *J. Phys. Chem. Lett.*, 2016, **7**, 3683–3689.
- 33 R. D. King-Smith and D. Vanderbilt, *Phys. Rev. B: Condens. Matter Mater. Phys.*, 1993, **47**, 1651–1654.
- 34 H. A. Kramers, *Proc. R. Acad. Sci. Amsterdam*, 1930, **33**, 959.
- 35 T. Etienne, E. Mosconi and F. De Angelis, *J. Phys. Chem. Lett.*, 2016, **7**, 1638–1645.
- 36 K. Wu, J. Chen, H. Ma, L. Wan, W. Hu and J. Yang, *Nano Lett.*, 2021, **21**, 740–746.
- 37 J. Nitta, T. Akazaki, H. Takayanagi and T. Enoki, *Phys. Rev. Lett.*, 1997, **78**, 1335.
- 38 A. D. Caviglia, M. Gabay, S. Gariglio, N. Reyren, C. Cancellieri and J. M. Triscone, *Phys. Rev. Lett.*, 2010, **104**, 126803.
- 39 S. Gupta and B. I. Yakobson, *J. Am. Chem. Soc.*, 2021, **143**, 3503–3508.
- 40 S. Babaee Touski and N. Ghobadi, *Phys. Rev. B: Condens. Matter Mater. Phys.*, 2021, **103**, 165404.
- 41 E. S. Park, D. J. Lee, O. J. Lee, B. C. Min, H. C. Koo, K. W. Kim and K. J. Lee, *Phys. Rev. B: Condens. Matter Mater. Phys.*, 2021, **103**, 134405.
- 42 Q. Liu, X. Zhang, J. A. Waugh, D. S. Dessau and A. Zunger, *Phys. Rev. B: Condens. Matter Mater. Phys.*, 2016, **94**, 125207.
- 43 C. Cheng, J. T. Sun, X. R. Chen, H. X. Fu and S. Meng, *Nanoscale*, 2016, **8**, 17854–17860.
- 44 W. Zhou, J. Chen, B. Zhang, H. Duan and F. Ouyang, *Phys. Rev. B: Condens. Matter Mater. Phys.*, 2021, **103**, 195114.